

Analysis and Use of fMRI Response Delays

Ziad S. Saad,^{1,2} Kristina M. Ropella,¹ Robert W. Cox,² and Edgar A. DeYoe³

¹Department of Biomedical Engineering Marquette University, Milwaukee, Wisconsin

²Biophysics Research Institute, Medical College of Wisconsin, Milwaukee, Wisconsin

³Department of Cell Biology, Neurobiology and Anatomy, Medical College of Wisconsin, Milwaukee, Wisconsin

Abstract: In this study, we implemented a new method for measuring the temporal delay of functional magnetic resonance imaging (fMRI) responses and then estimated the statistical distribution of response delay evoked by visual stimuli (checkerboard annuli) within and across voxels in human visual cortex. We assessed delay variability among different cortical sites and between parenchyma and blood vessels. Overall, 81% of all responsive voxels showed activation in phase with the stimulus while the remaining voxels showed anti-phase suppressive responses. Mean delays for activated and suppressed voxels were not significantly different ($P < 0.001$). Cortical flat maps showed that the pattern of activated and suppressed voxels was dynamically induced and depended on stimulus size. Mean delays for blood vessels were 0.7–2.4 sec longer than for parenchyma ($P < 0.01$). However, both parenchyma and blood vessels produced responses with long delays. We developed a model to identify and quantify different components contributing to variability in the empirical delay measurements. Within-voxel changes in delay over time were fully accounted for by the effects of empirically measured fMRI noise with virtually no measurable variability associated with the stimulus-induced response itself. Across voxels, as much as 47% of the delay variance was also the result of fMRI noise, with the remaining variance reflecting fixed differences in response delay among brain sites. In all cases, the contribution of fMRI noise to the delay variance depended on the noise power at the stimulus frequency. White noise models significantly underestimated the fMRI noise effects. *Hum. Brain Mapping* 13:74–93, 2001. © 2001 Wiley-Liss, Inc.

Key words: MRI methods/techniques; activation latency; human visual cortex; angiography noise

INTRODUCTION

Functional magnetic resonance imaging (fMRI) has become an increasingly popular technique for studying brain activation in response to sensory, motor, or

cognitive events. fMRI responses that are time-locked to a regular alternation of experimental and control stimuli (or tasks) can be detected using various techniques such as temporal cross-correlation, statistical parametric mapping, and principal components analysis [Friston et al., 1990; Bandettini et al., 1993; Forman et al., 1995; Strother et al., 1995; Backfrieder et al., 1996]. Although the time course of the fMRI signal is typically used to assist detection of valid fMRI responses, the temporal delay of the response, itself, may be an important focus of interest. However, the delay of the fMRI response does not directly depict the timing of the underlying neural activation. Rather, it

Contract grant sponsor: NIH; grant numbers: EY10244, MH51358, GCRC1234.

Correspondence to: Dr. E.A. DeYoe, Dept. of Cell Biology, Neurobiology and Anatomy, Medical College of Wisconsin, 8701 Watertown Plank Rd., Milwaukee, WI 53226-0509.

E-mail: deyoe@mcw.edu

Received for publication 11 February 2000; accepted 31 January 2001

reflects the temporal properties of both the neural events and the rather sluggish hemodynamic components of the blood oxygenation level dependent (BOLD) mechanism [DeYoe et al., 1994]. Consequently, the study of fMRI response delays is important for determining the limitations of fMRI in resolving the chronology of brain activation. In this latter respect, fMRI response delays have been used to resolve different stages of brain processing [Rao et al., 1995] and to depict mental chronometry [Menon et al., 1998]. Moreover, the fMRI response delay is the primary parameter of interest in a technique termed “temporal phase mapping,” used previously to map the visual and auditory organization of human cerebral cortex [Engel et al., 1993, 1994, 1997; Sereno et al., 1995; DeYoe et al., 1996]. Despite this interest, a detailed description of the variability of the fMRI response delay has been lacking, thus leaving uncertainty concerning the accuracy of timing-based fMRI response measures.

It is often assumed that all fMRI voxels have the same response delay, that is, that they are time and space invariant. However, examinations of empirical fMRI data have revealed variations in response delay of several seconds [Lai et al., 1993; Lee et al., 1995; Saad et al., 1995; Kruggel and von Cramon, 1999a, 1999b]. Such variation was found in repeated measurements from single voxels and in simultaneous measurements across voxels at different brain sites. This relatively wide range of response delays has been attributed to the delayed flow of oxygenated blood through large veins draining the sites of neuronal activation [Lai et al., 1993; Lee et al., 1995]. However, such variation could also reflect spatial and temporal heterogeneity in neuronal or hemodynamic function and anatomy, or could simply reflect the presence of fMRI noise [Weisskoff et al., 1993; Biswal et al., 1995, 1996; Mitra et al., 1997; Saad et al., 1997b, 1997c; Kruggel and von Cramon, 1999a, 1999b]. The relative importance of each of these factors is not known.

Finally, previous work has shown that most activated voxels respond temporally “in phase” with the time course of a stimulus, though others are modulated “out of phase” or “antiphase.” Such responses have been alternately attributed to neuronal or hemodynamic factors, or imaging artifacts [Seitz et al., 1990; Seitz and Roland, 1992; Jesmanowicz et al., 1993; Haxby et al., 1994; Lee et al., 1995; Saad et al., 1995]. Their true origin remains uncertain and more detailed data are needed to help settle the controversy.

To address these issues, we implemented an efficient algorithm for measuring response delays in fMRI data and used it to estimate the delay variance across

time and space and for parenchyma versus blood vessels. These empirical observations are described below in Part I. We then estimated the effect of fMRI noise on the delay variance and proposed a model for parceling the sources contributing to the variance of the empirical delay estimates. The model was used to estimate the delay variability in time and space of stimulus-induced fMRI responses without the contamination of fMRI noise. These observations are described in Part II. Preliminary reports of this work have appeared previously [Saad et al., 1995, 1996, 1997a, 1997b, 1997c, 1999a, 1999b; Saad, 1996].

PART I: EMPIRICAL METHODS

Subjects

Data were collected from four male and three female subjects (21–42 years) with no metallic implants and no known neurological or visual deficits. Subjects read and signed a detailed consent form describing the experimental procedures as approved by an internal review board. Prior to data collection, subjects were trained to position their head in a model of the gradient head coil, adjust the custom optical system to allow viewing of the video images, and perform the visual task while constantly fixating on a point in the center of the visual field.

Visual stimuli

High-quality visual stimulation was achieved using a custom optical system designed to project images directly onto the retinae of subjects, thereby providing high-luminance, a 60° field of view, and minimizing the effects of changes in pupillary size [DeYoe et al., 1994]. Custom computer graphical images were generated using a Cambridge Instruments VSG 2/3 video card and displayed via a Sharp XG2000U color LCD video projector driven by a microcomputer. A variable, neutral density, polarizing filter was used to adjust the average luminance of the images to a comfortable photopic range for each subject.

The visual stimulus consisted of a black and white checkered annulus (approximate contrast 97%) counterphase flickered at 8 Hz, centered on a fixation point (Fig. 1A) [DeYoe et al., 1994]. The stimulus background was equiluminant gray in all but the first three cases (CL, CM, and DM) where it was black. Check size was scaled with eccentricity. To stimulate different retinotopic zones, we used annuli having average eccentricities of 3° (range 1.7°–4.3°), 9° (range 5°–13°),

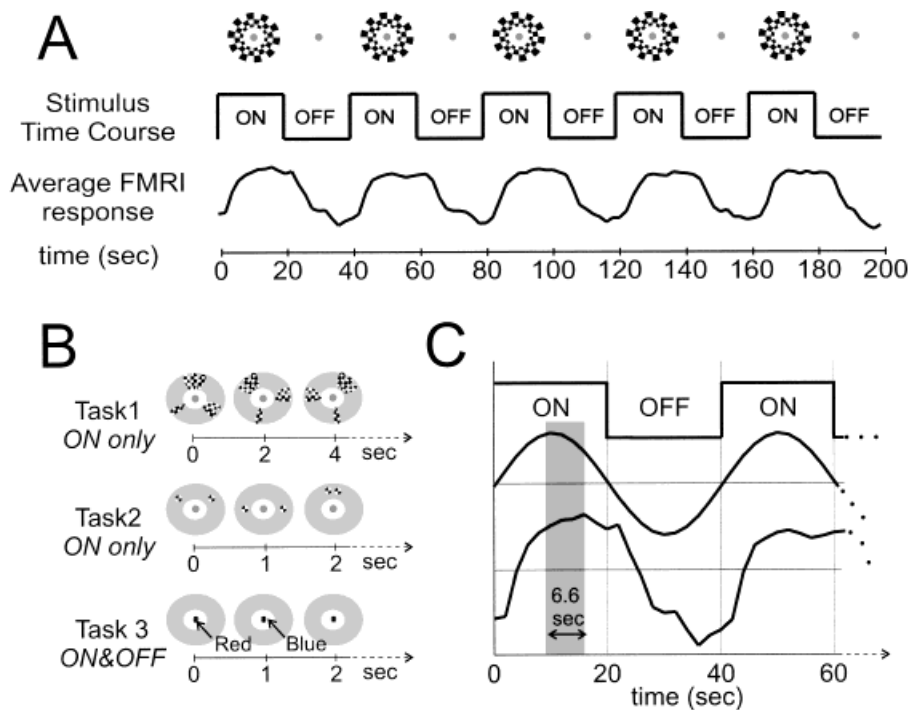


Figure 1.

Experimental paradigm for visual stimulus and delay response measurement. **(A)** Visual stimuli consisted of flickering checkered annuli presented for 20-sec (ON) periods alternating with equal periods of fixation point alone (OFF) for five ON/OFF cycles. **(B)** Behavioral tasks: Task 1, subjects determined if the target pattern had been rotated or mirrored. Task 2, subjects determined if the targets moved closer to, or farther away from, the 12-o'clock position. Task 3, subjects determined whether a marker at the fixation point changed between red and blue colors. **(C)** Example showing time delay (gray shading) of fMRI response (bottom) relative to ideal sinusoidal response (middle) and stimulus time course (top).

and 24° (range 13.3°–34.7°). The size and eccentricity of the annulus was constant throughout an individual fMRI scan. A stimulus cycle was defined as the period during which the stimulus was presented (ON period) followed by the period during which the stimulus was turned off (OFF period).

Subjects were required to maintain gaze on the fixation point throughout the scan. To guarantee that attention was concurrently directed to the stimulus pattern, subjects were required to perform a visual task during the ON periods (tasks 1 and 2) or during both ON and OFF periods (task 3). Figure 1B illustrates the three types of visual tasks presented.

In the first task, three target groups consisting of one, two, or three ellipses that were superimposed at equally spaced positions around the checkered annulus [DeYoe et al., 1996]. The subject performed a one-back comparison to determine whether the target pattern on each successive presentation had been simply rotated, or both mirrored and rotated about the fixation point.

In the second task, two targets consisting of checkered dots were superimposed on the annulus at equal angular distances from the 12-o'clock position. During successive ON periods, subjects determined whether the target dots moved closer to, or farther away from, the 12-o'clock position. Subjects indicated their decisions by activating one of two manual switches.

During the OFF periods in tasks 1 and 2, subjects performed sham responses by randomly pressing one of the two manual switches at approximately the same rate as during the ON period.

In the third task, the stimulus consisted of the checkered annulus and a thin colored line overlaid on the fixation point. During both ON and OFF periods, subjects were required to determine whether the thin line contained within the fixation point changed between red and blue colors.

Seventy-five of 89 data sets were obtained using a stimulus completing five cycles in 200 sec (1/40 Hz). To study the effects of stimulus cycle frequency on the distribution of response delays, we collected fourteen additional data sets using faster (1/28 Hz) and slower (1/64 Hz) stimulus cycles.

To obtain an estimate of the fMRI signal variation in the absence of a stimulus, control scans were also obtained in which only the fixation point was presented against a uniform gray field of the same average luminance as the checkered annuli. For these scans, subjects passively gazed at the fixation point.

To reduce motion artifacts, all images in the fMRI time series were registered to a set of reference echo planar images [Cox and Hyde, 1997]. The reference echo planar images were selected from fMRI data sets acquired immediately before or after the high-resolution anatomical or angiography data sets.

Scanner and pulse sequence

Brain images were obtained with a 1.5 T General Electric Signa scanner equipped with a custom three-axis, shielded head coil designed for rapid gradient field switching [Wong et al., 1992]. The spatial resolution was set by a 64×64 voxel matrix covering a 24×24 cm field of view with a slice thickness of 4–8 mm. This gave an in-plane resolution of 3.75×3.75 mm. The pulse sequence used during image acquisition was a gradient-recalled EPI sequence with an initial 90° RF pulse, an effective echo time (TE) of 40 ms, and an image repetition rate (TR) of 2 sec [DeYoe et al., 1994]. A typical scan sequence consisted of a series of images ($N = 102$ – 110) of (10–20) contiguous slices covering most of the brain. The first two images of the scan series were discarded to allow brain tissue magnetization to achieve steady state. The remaining images (100–108) in the scan sequence constituted the functional data set used to create the functional images. The mean and linear trends were removed from each of the voxel time series by linear regression. In all but three of the 87 data sets obtained with the active visual stimulus, the scan sequence was repeated 2–3 times for image averaging. In the remaining three data sets the scan sequence was performed only once. During the scanning session, control scans were interspersed with active scans.

During each scanning session, a high-resolution, T1-weighted, spoiled GRASS (gradient recalled acquisition in steady state) anatomical data set was collected to localize functional activity and to create a triangularly tessellated computer model of the surface of the brain. The anatomical data set covered the whole brain at a resolution of $0.94 \times 0.94 \times (1.0$ – $1.2)$ mm. In addition, for three of the subjects, an MR 2D time-of-flight (2D-TOF) angiography data set was collected using a vascular spoiled GRASS sequence (flip angle = 50° , TR = 45 ms, FOV = 24 cm) with voxel size of $0.94 \times 0.94 \times 1.5$ mm. This pulse sequence was optimized for cortical venous mapping and was sensitive to slow flow states [GE Medical Systems, 1990].

Active voxel detection and estimation of response delays

This stage of analysis involved detecting voxels activated by the visual stimulus and estimating their response delay relative to the stimulus time course. This was accomplished using a modified cross-correlation technique whereby the fMRI time series for each voxel is cross-correlated with a reference time series approximating the fMRI response to the stimulus.

This cross-correlation technique assumes that the reference time series $r(t)$ and the fMRI time series $s(t)$ are modeled by the following set of equations [Bendat and Piersol, 1986].

$$r(t) = x(t) + m(t)$$

$$s(t) = y(t) + n(t) = \alpha x(t - \Delta t) + n(t) \quad (1)$$

where the reference time series $r(t)$ is comprised of $x(t)$, the ideal fMRI response, and a noise component $m(t)$. The fMRI response $s(t)$, is comprised of a scaled (α), and time-shifted (Δt) version of $x(t)$ plus a noise component, $n(t)$. Assuming that the noise components $m(t)$ and $n(t)$ have zero mean and are uncorrelated with $x(t)$ and with each other, the cross-correlation coefficient function $R_{rs}(\tau)$ for different delays between $r(t)$ and $s(t)$ is reduced to:

$$R_{rs}(\tau) = \alpha R_{xx}(\tau - \Delta t) \quad (2)$$

$R_{xx}(\lambda)$ is the autocorrelation of $x(t)$ and is maximal when $\lambda = 0$. Consequently, $R_{xx}(\tau - \Delta t)$ is maximal when $\tau = \Delta t$. Thus by determining the delay τ at which $R_{rs}(\tau)$ is maximal, we can estimate the delay Δt between $r(t)$ and $s(t)$ as well as the maximal cross-correlation coefficient $\rho(\Delta t)$ defined by:

$$\rho(\Delta t) = \frac{R_{rs}(\Delta t)}{\sqrt{R_{rr}(0)R_{ss}(0)}} \quad (3)$$

Each voxel was considered activated when the cross-correlation coefficient $\rho(\Delta t)$ was larger than a predetermined threshold value $\rho_t = 0.50$, corresponding to a false positive probability less than 0.0001 for each voxel after a Bonferroni correction [Johnson and Wichern, 1992; Saad, 1996]. For these experiments, the reference time series $r(t)$ consisted of a sinusoid having a frequency equal to the stimulus cycle frequency. Thus the noise component $m(t)$ was null and $r(t) = x(t)$. Overall, in our data the sinusoid was correlated with the average fMRI response at a level of 0.97, thereby indicating that it was a good approximation.

Because of the discrete nature of $r(t)$ and $s(t)$, the determination of $\rho(\Delta t)$ and Δt at a time resolution smaller than the sampling interval requires difficult nonlinear curve fitting as neither the maximum value of $\rho(\tau)$ nor the value of Δt are known. In addition, the estimation of $\rho(\tau)$ in the time domain requires convolution between reference and fMRI time series and thus is computationally inefficient. To overcome these difficulties, we applied a computationally efficient al-

gorithm that used the Hilbert transform (H[.]) [Bendat et al., 1986; Bendat and Piersol, 1993] to obtain high-resolution time delay estimates. These estimates were also used to compute the variance of the delays across voxels. The algorithm, described in the appendix, included the computations required by the cross-correlation technique and was used to detect activated voxels without additional computational costs.

The activated voxels were split into two complimentary groups based on the polarity of their response. Voxels were considered positive (in phase) when the fMRI signal increased from baseline level approximately coincident with the onset of the stimulus. Conversely, voxels were considered negative (antiphase) when the fMRI signal decreased from baseline with stimulus onset. Mean delays and variances were computed separately for each of the two groups. Voxel delay was represented on the corresponding brain maps according to a circular pseudocolor scale.

Separation of voxels into vascular and parenchymal pools

To determine the difference in activation delays between large blood vessels and parenchyma, we used two methods to classify activated voxels as vessel or parenchyma related.

In the first method, we imaged blood vessels directly using 2D-TOF sequence capable of resolving blood vessels greater than 2 mm in diameter. To isolate blood vessels from other tissue, we applied an image intensity threshold (I_t) followed by a 3D-cluster volume threshold of $10 \mu\text{l}$, the equivalent of 8 contiguous voxels. 2D-TOF voxels that exceeded I_t and formed clusters larger than $10 \mu\text{l}$ were categorized as blood vessels. Figure 2 shows 3D renderings of segmented 2D TOF angiography from one subject at liberal, medium, and conservative I_t . With $I_t = 0.2$, most vessels detectable by 2D-TOF were identified; however, the segmentation was noisy and the likelihood of falsely classifying parenchymal tissue as blood vessels was high. Conversely, with $I_t = 0.8$, only large vessels were identified and the likelihood of classifying parenchymal tissue as blood vessels was low. fMRI voxels were ascribed to the vasculature pool if they spatially overlapped with blood vessel voxels by more than a preset threshold (O_t). We considered overlap thresholds ranging from 0.01% (minimal overlap) to 50%. Because voxel classification was dependent on the arbitrary thresholds I_t and O_t , we repeated the comparison of delay distributions at (I_t , O_t) combinations ranging from (0, 0.01%) to (1, 50%). The Student's t test and F test were used to compare delay mean and

variance between voxels in the vascular pool and those in the parenchymal pool. The analysis was performed for 12 data sets, obtained from three subjects with a stimulus cycle duration of 40 sec.

In the literature, an alternate technique for identifying blood vessels assumes that they are associated with large signal changes [Lai et al., 1993; Menon et al., 1993, 1998; Ogawa et al., 1993; Lee et al., 1995]. Consequently, we attempted to isolate blood vessels from parenchyma using the normalized signal change defined as $S_n = 100 \times (\text{ON-OFF})/\text{OFF}$. Because the threshold criterion separating these two groups was arbitrary, we computed mean delay difference at various thresholds covering the range of observed S_n . We then sought to determine the largest significant difference in mean delay between voxels with high versus low S_n , thereby identifying the largest difference in mean delay between blood vessels and parenchyma.

Response delay variability within voxels

Much of our analysis focused on the variability in response delays across voxels (σ_{across}^2). However, the response delay at a specific voxel can also vary over time. To estimate this within-voxel delay variance (σ_{within}^2), we repeated the same fMRI scan multiple times during the same experimental session ($N_{\text{rep}} = 12, 14, \text{ and } 20$ for experiments NY, OU, and OW, respectively). The stimulus cycle duration was 40 sec. The within-voxel variance was estimated from the response delays for individual voxels across scan repetitions in which the voxels were activated. Voxels that were activated in less than four out of the N_{rep} scan repetitions were not considered. This ensured a match between the mean SNR of the pool of voxels used in estimating σ_{within}^2 and that of the voxels used in estimating σ_{across}^2 . The estimated within-voxel variance (σ_{within}^2) for the entire data set was the average of the variances estimated at each activated voxel.

PART I: EMPIRICAL RESULTS

Response delay variability across voxels

Figure 1C illustrates the relative timing between the visual stimulation (top), the reference time series

Figure 2.

3D rendering of segmented 2D time-of-flight angiography obtained with a vascular Spoiled GRASS sequence optimized for cortical venous mapping. Blood vessels (red) were segmented using image intensity threshold (I_t) and a volume cluster threshold of $10 \mu\text{l}$. The three renderings show the segmented vessels at low (0.2), medium (0.4), and high (0.8) I_t . P.O.S. = parieto occipital sulcus.

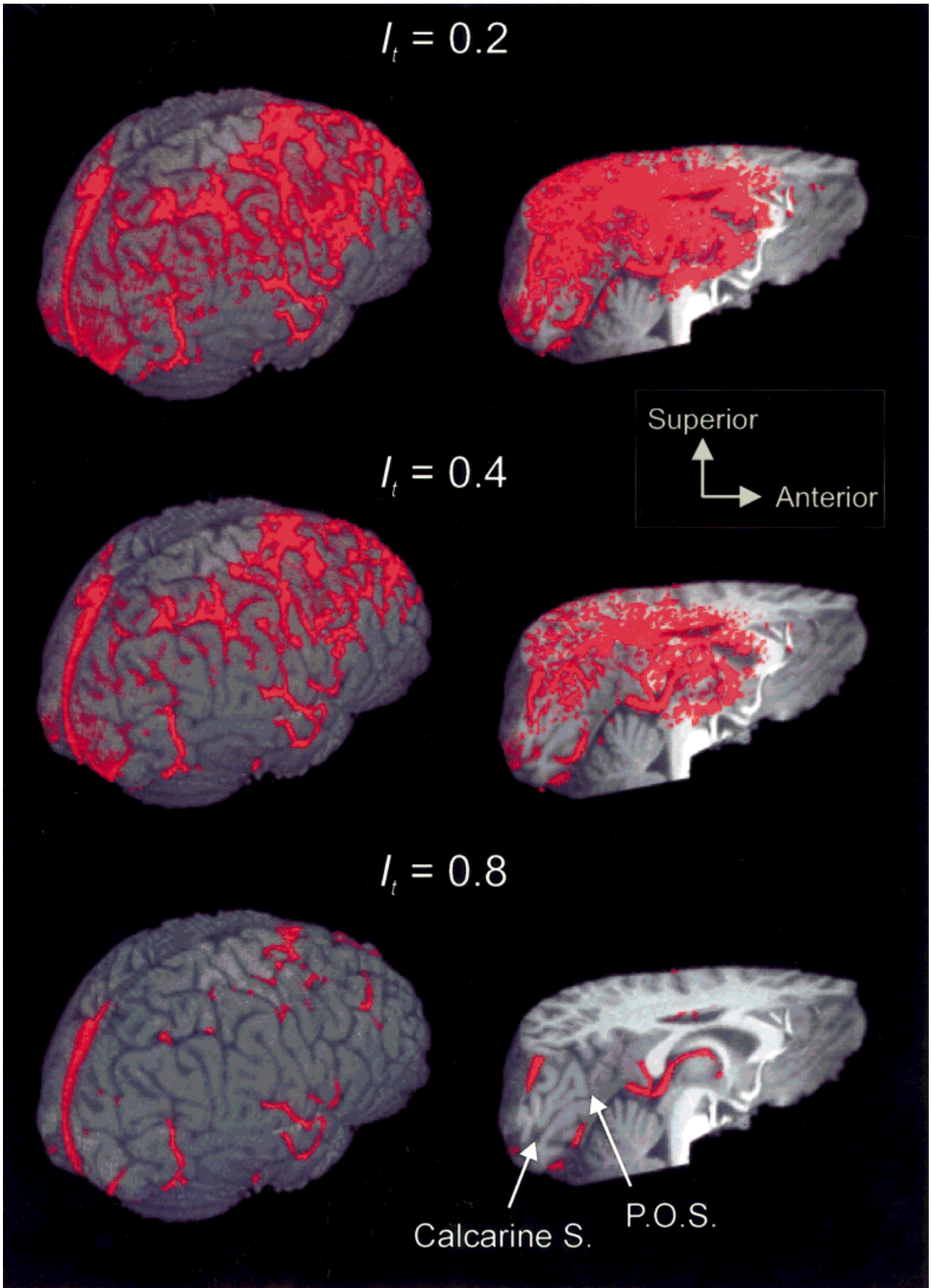


Figure 2.

(middle), and the fMRI response (bottom). The reference time series represents an ideal fMRI response with no response delay. In this example, the average fMRI response across activated voxels is delayed by 6.6 sec (gray shading) relative to the reference waveform.

The distribution of response delays for all active voxels in a representative single scan is illustrated in Figure 3 (A,C,E). Figure 3 (B, D, F) shows the average waveforms for the fMRI responses for all active voxels. The results are compared for three different stimulus cycles ($T_{\text{ON-OFF}}$) corresponding to ON/OFF periods of 64 (A,B), 40 (C,D), and 28 (E,F) sec, respectively. The average waveform for negative responses tended to be slightly noisier than for positive responses, probably as a result of the smaller number of voxels contributing to the average. Note the decrease in the total number of activated voxels (N) with decreasing stimulus cycle duration.

For each subject and each of the three stimulus cycle durations, both positive (+, black) and negative (–, gray) responses were observed. Figure 3D shows that for positive voxels, the fMRI signal increased from baseline coincident with the onset of the stimulus. However, for negative voxels, the fMRI signal decreased from baseline with stimulus onset. The latter observation, in agreement with Lee and colleagues [1995], indicates that the fMRI responses associated with negative voxels are not caused by excessively delayed activation. Rather, negative fMRI responses are primarily the result of suppression of the fMRI signal occurring simultaneously with activation of positive voxels.

On average across all subjects, 81% of the activated voxels had positive responses. However, the proportion varied for individual subjects and stimulus cycle durations. All data sets contained at least some voxels having negative responses and, in some data sets, this latter group accounted for up to 50% of the activated voxels. Overall, the mean negative response delays did not differ significantly from their positive counterparts (t test, $P < 0.001$). For positive responses, the mean of the response delays did not vary significantly (ANOVA, $P < 0.01$) across cycle durations: 8.50, 8.00, 9.27 sec (Table IA) for cycle durations of 28, 40, and 64 sec, respectively. In contrast, the variance of the delays (σ_{across}^2) increased considerably with increasing cycle durations. In all but one of the 21 pairs of data sets compared, this increase was significant (F-ratio test, $P < 0.01$). The exception was one pair of data sets (28- and 40-sec cycle duration) where the variance increase was significant at $P < 0.03$. On average, the variance increased from 2.53 to 4.36 to 23.46 sec² (Table IB).

One concern was that negative responses might reflect differences in the focus of attention (periphery versus fixation) for ON versus OFF periods. Therefore, we repeated the delay analysis for three subjects using a task in which the subject was required to detect a change in color at the fixation point continuously throughout the scan. The resulting data did not differ from that obtained with the other tasks.

Spatial distribution of response delays

Figure 4 shows an example of the spatial distribution of response delays on unfolded maps of occipital cortex for one representative subject out of three. The data shown in the different maps of Figure 4 were obtained using annular checkerboards having mean eccentricities of 3°, 9°, and 24°, and a stimulus cycle duration of 40 sec.

In the central portion of the maps (along the calcarine sulcus), the distribution of positive (yellow-red) and negative (blue-green) responses varied depending on the size (eccentricity) of the checkered annulus. This zone encompassed the most strongly retinotopic visual areas (V1, V2, V3, VP, V4). In this region, iso-eccentricity contours (not illustrated, see DeYoe et al., 1996) representing a fixed eccentricity in the visual field run nearly perpendicular to the calcarine sulcus in a manner virtually identical to the obvious boundary between positive and negative responses visible in the left and right maps. Thus, in this region the distribution of positive and negative responses appears to be highly dynamic and reflects the spatial configuration of the stimulus. For example, voxels located in the middle of the calcarine sulcus had negative response delays for the 3° annulus but had positive response delays for the 24° annulus. Note also that the transition from positive to negative responses was typically abrupt rather than smoothly graded. For visual areas outside this region, retinotopy is not as strong and the distribution of positive and negative responses appears more constant.

Mean response delays varied significantly (t test, $P < 0.01$) by as much as 1.35 to 2 sec across different visual areas [DeYoe et al., 1994, 1996]. However, such differences did not seem to reflect any likely connective hierarchy, nor did they appear to be related to neuronal latencies, which are reported to differ by only a few tens of milliseconds across visual areas [Buchner et al., 1994; Bullier et al., 1996; Nowak and Bullier, 1997; Schmolesky et al., 1998].

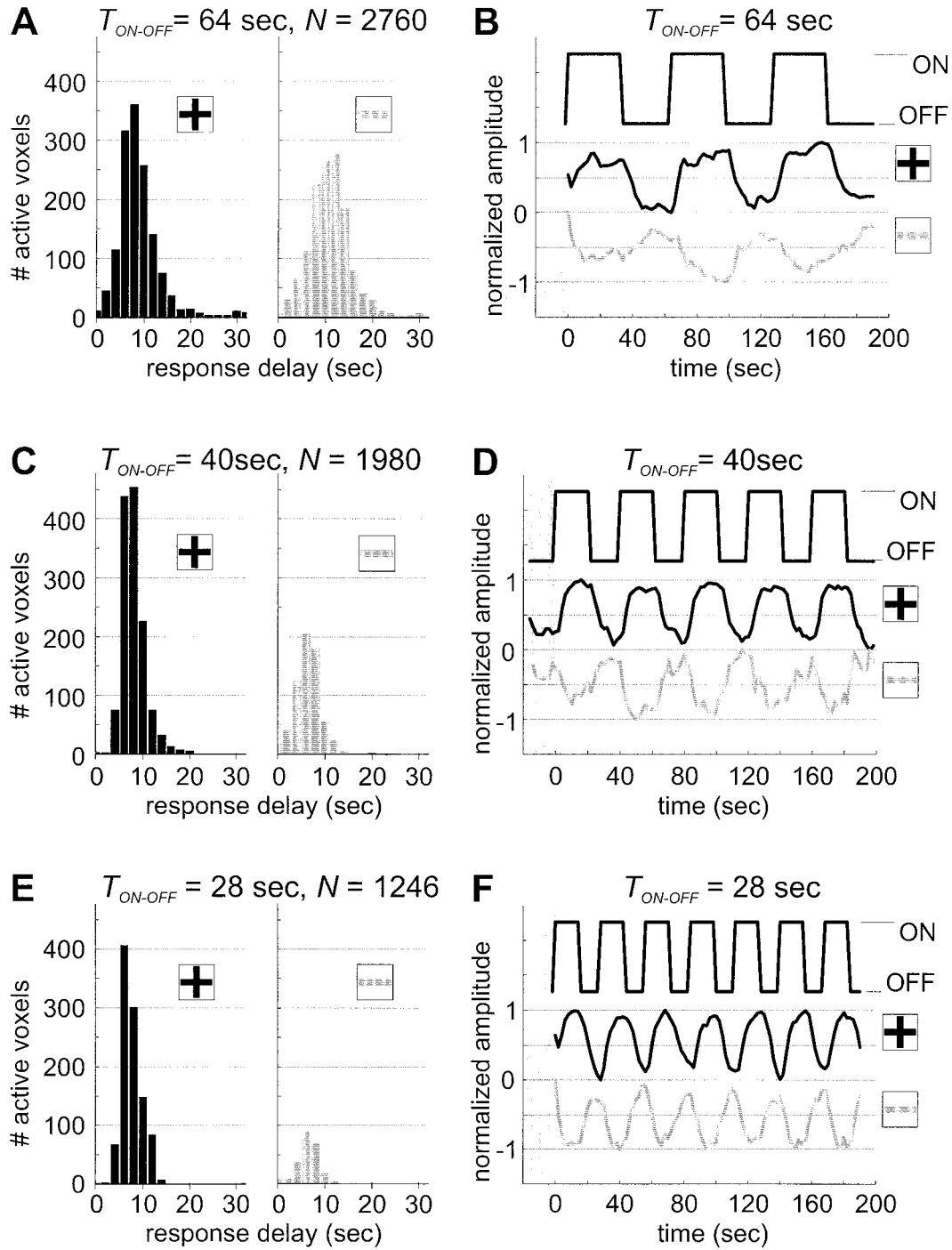


Figure 3.

(**A, C, E**): Response delay distributions for positive (+ black) and negative (– gray) responses obtained for stimulus cycle durations (T_{ON-OFF}) 28, 40, and 64 sec. (**B, D, F**): Examples of stimulus presentation time course (top), average positive (middle), and

negative (bottom) fMRI responses. Gray shading in (**D**) highlights fMRI baseline signal during 20-sec prestimulus period. Note that negative responses are suppressed below prestimulus baseline.

TABLE I. Mean and variance of fMRI response delay

	Stimulus cycle ($T_{\text{ON-OFF}}$)		
	28 sec	40 sec	64 sec
A- Mean delay (sec)	8.50	8.00	9.27
B- Delay variance (sec²)			
Across voxels (σ_{across}^2)	2.53	4.36	23.46
Within voxels (σ_{within}^2)	—	1.44	—
FMRI noise ($\sigma_{\text{FMRI noise}}^2$)	0.54	1.45	4.25
Stimulus, time ($\sigma_{\text{Stim,time}}^2$)	—	0	—
Stimulus, space ($\sigma_{\text{Stim,space}}^2$)	1.99	2.91	19.21

A- Mean delay of the fMRI response at three stimulus cycle durations. B- Factors contributing to the variance in the delay of the fMRI response. σ_{across}^2 , σ_{within}^2 , $\sigma_{\text{FMRI noise}}^2$ were measured using empirical fMRI data. $\sigma_{\text{Stim,time}}^2$ and $\sigma_{\text{Stim,space}}^2$ were inferred using equations 4 and 5 in the text.

Response delays for large blood vessels vs. parenchyma

We used 2D-TOF data to categorize voxels as blood vessels and parenchyma. Figure 5A shows normalized histograms of the response delay for the two pools. Overall, the mean delay for blood vessels was slightly longer than the mean delay for parenchyma. However, given the variability of the delays, these differences were not consistently significant (t test, $P < 0.01$) for all subjects and threshold criteria. Moreover, in all three subjects, the variance of the delay distributions showed no consistent difference between the vascular and parenchymal pools.

Because the threshold criteria for classifying voxels as blood vessels were arbitrary, we examined the delay differences across a wide range of criteria. Figure 5B shows the difference in mean delay over a range of the intensity threshold criterion I_t (dark line). The delay difference tended to increase as the criterion for identifying blood vessels (I_t) became more stringent. In two out of three subjects, this trend was statistically significant ($P < 0.01$) [Hogg and Ledolter, 1987]. We also examined this trend over the secondary criterion, the overlap threshold (O_t), and found a similar trend for values of O_t ranging from 0.01% to 50% (thin lines). Overall, the delay differences varied significantly across subjects and threshold criteria. So, to estimate the maximum possible delay difference between blood vessels and parenchyma, we selected the optimal criteria separately for each subject. The resulting maximum delay differences (asterisks) of 1.76, 2.37, and 0.67 sec were significant (t test, $P < 0.01$) for each of the three subjects respectively.

In the literature [Lai et al., 1993; Menon et al., 1993, 1998; Ogawa et al., 1993; Lee et al., 1995], an alternate technique for identifying blood vessels has been proposed whereby blood vessels are purported to exhibit large normalized signal change (S_n). We used this alternate to the 2D-TOF technique to obtain another estimate of the delay difference between blood vessels and parenchyma. Figure 6 shows scatter plots of delay versus normalized signal change (S_n) from the two most disparate subjects. The horizontal line separating the voxels into high (Hi) and low (Lo) S_n was selected to maximize the difference in mean delay between the high and low pools. The resulting mean delays for each pool are indicated by the respective markers on the abscissa. For three subjects, the maximal significant (t test, $P < 0.01$) difference in mean delay between voxels with high and low S_n was 1.43 sec (range: 0.81–2.17 sec). The cases in Figure 6 represent the extremes of this range. Note that these delay differences were consistent with results from our 2D-TOF analysis. Also note that there was no criterion using this technique for which the delay distributions did not completely overlap.

Response delay variability within voxels

One source of variation in response delay across a sample of voxels may be fixed differences in response from one brain site to another (σ_{across}^2). However, another source of delay variability can be random, or even systematic, changes in response delay over time. Consequently, we performed an analysis of the within voxel variance for a total of 41 repeated scans from two subjects (ZS, 6 and 20 scans; KR, 15 scans) with a stimulus cycle of 40 sec. The mean within-voxel variance, σ_{within}^2 was 1.44 sec² (range: 1.28–1.60).

PART II: SIMULATION METHODS

For any given voxel, the time course of the BOLD signal can be attributed to both stimulus-driven (Stim) and nonstimulus factors. Stimulus-driven changes are caused by, or correlated with, the presentation of the stimulus. In general the stimulus-related responses may vary from one presentation to the next ($\sigma_{\text{Stim,time}}^2$) and from location to location within the brain ($\sigma_{\text{Stim,space}}^2$). Neither of these sources of variance can be measured directly because they are always combined with variance as a result of noise. fMRI noise includes nonstimulus changes caused by a variety of factors including respiration, heart beat, thermal

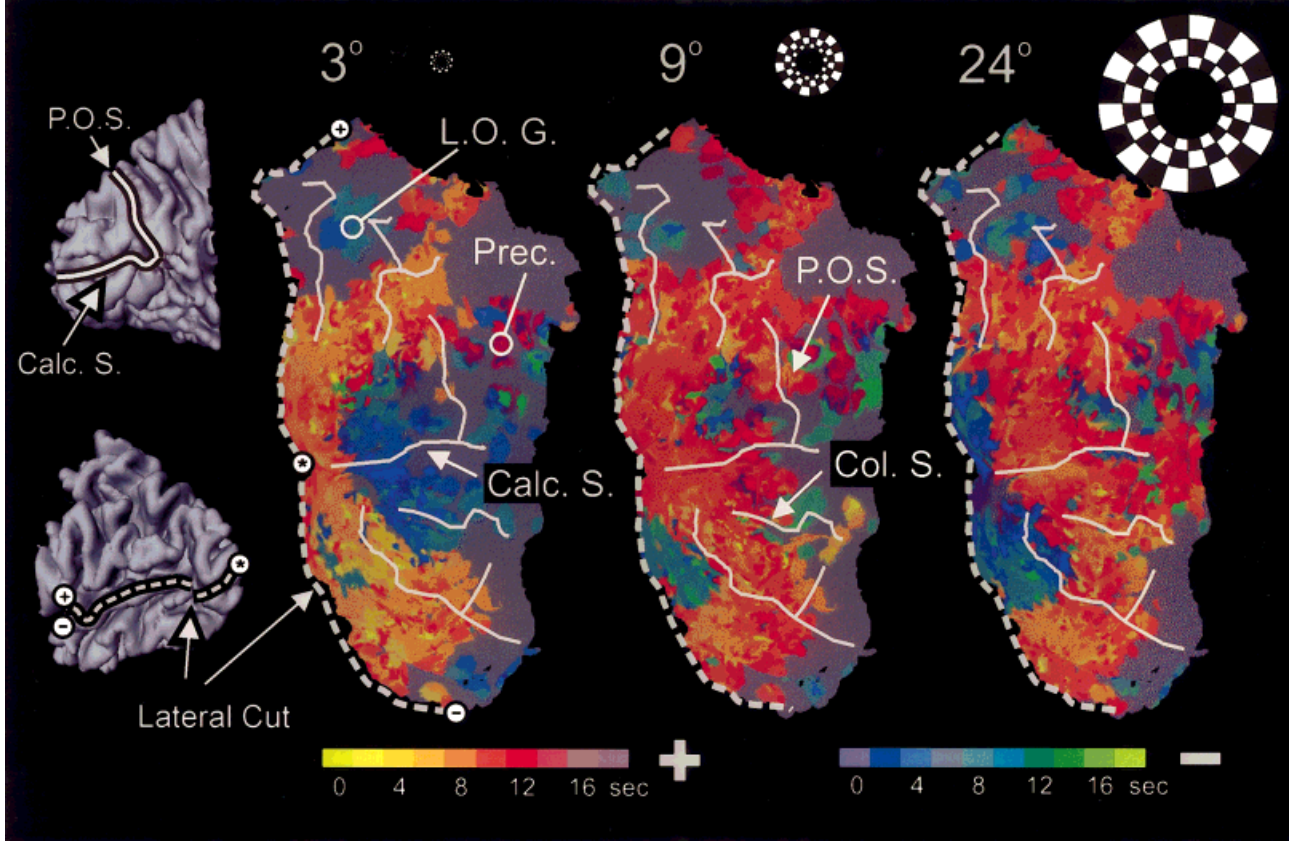


Figure 4.

Two-dimensional (2D) flat maps of occipital cortex showing spatial distribution of response delays represented by circular pseudocolor code indicated at bottom. Each map shows the delay pattern for checked annuli of different mean radii (3°, 9°, and 24°). Dotted line marks edges of the cut made in 3D tessellated surface to permit flattening. The asterisk marks the location of the occipital pole on the 3D and 2D surfaces. The + and - symbols mark

the cortical surface superior and inferior to the anterior tip of the lateral cut. Yellows and reds represent delays for positive fMRI responses, blues and greens represent delays for negative fMRI responses. Calc. S. = calcarine sulcus; Col. S. = collateral sulcus; P.O.S = parieto occipital sulcus; L.O.G = lateral occipital gyrus; Prec. = Precuneus.

noise, and additional fluctuations that have unidentified physiological origins [Weisskoff et al., 1993; Biswal et al., 1995, 1996].

Figure 7 summarizes the sources of variance in the empirical estimates of response delay. In Part I, we described empirical estimates of the delay variance across a population of voxels, σ_{across}^2 , and for repeated measures of the same voxels, σ_{within}^2 . In this section, we estimate the contribution of fMRI noise to the empirical estimates of delay variability. The latter component ($\sigma_{\text{fMRI noise}}^2$) depends on the degree to which fMRI noise encroaches on the bandwidth of the stimulus-induced fMRI response. If we can independently estimate the variance caused by fMRI noise, it should be possible to estimate the variance associated with the response to the stimulus itself.

Equations 4 and 5 formalize the preceding notions:

$$\sigma_{\text{within}}^2 = \sigma_{(\text{Stim,time})}^2 + \sigma_{\text{fMRI noise}}^2 \quad (4)$$

$$\sigma_{\text{across}}^2 = \sigma_{(\text{Stim,space})}^2 + \sigma_{(\text{Stim,time})}^2 + \sigma_{\text{fMRI noise}}^2 \quad (5)$$

where:

- $\sigma_{(\text{Stim,time})}^2$ is the delay variance associated with changes in the response to the stimulus from one presentation to the next.
- $\sigma_{\text{fMRI noise}}^2$ is the delay variance caused by fMRI noise.
- $\sigma_{(\text{Stim,space})}^2$ is the delay variance due to fixed differences in the stimulus-driven response from one brain location (voxel) to the next.

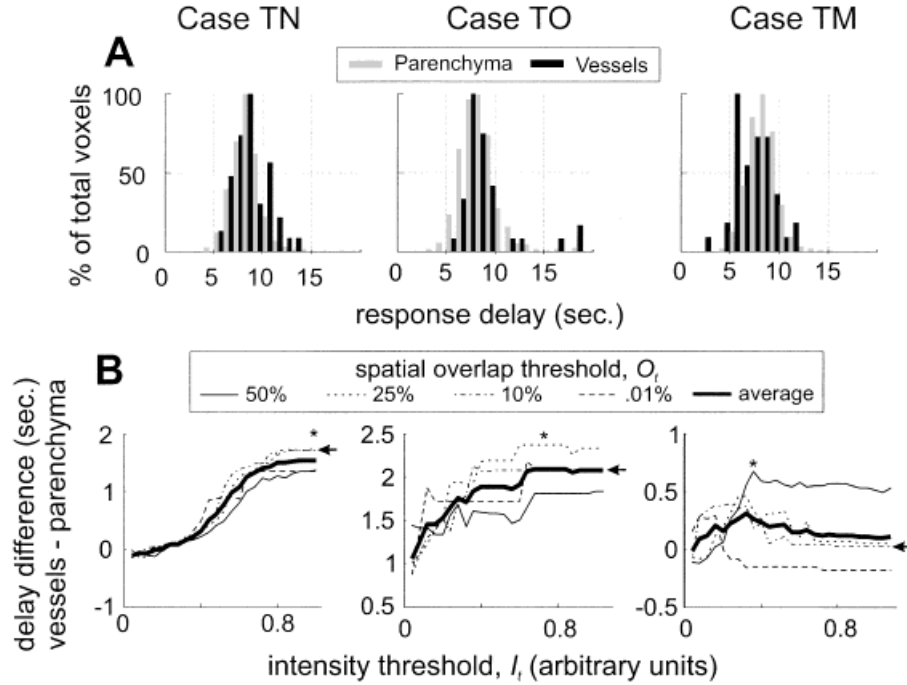


Figure 5.

(A) Normalized delay distributions for blood vessels (black) and parenchyma (gray) classified according to 2D-TOF data. Ten percent of activated voxels were mapped to blood vessels; however, the histograms were normalized to facilitate the comparison of the two distributions. Note that the variance of the vascular and parenchymal distributions showed no statistical difference. (B) Mean delay difference between voxels mapped to vessels and parenchyma vs. the intensity threshold criterion, I_t , for vessel segmentation. The thin lines show the delay differences at four

different overlap thresholds (O_t) and the thick trace is the average of all the thin traces (see Methods for details). Note in cases TN and TO that the delay difference increased ($P < 0.01$) as I_t , the criterion for identifying vessels, became stricter. Asterisks mark the largest differences in mean delay of 1.76 and 2.37 and 0.67 sec for cases TN, TO, and TM, respectively. Note the difference in the Y axis between the three graphs. Arrows indicate conditions ($I_t = 1$, $O_t = 10\%$) for which distributions in (A) were obtained.

In words, the within-voxel delay variance, σ_{within}^2 reflects moment-to-moment variations in the response to the stimulus plus fMRI noise. However, for a population of different voxels, the delay variance, σ_{across}^2 also reflects fixed differences in response from one brain location to another. Strictly speaking, these equations will be valid only if the delays caused by the stimulus-driven response and fMRI noise are independent random variables (implying zero covariance) [Hogg et al., 1987]. Lacking evidence to the contrary, we assume here that this is true.

In Part I, σ_{within}^2 and σ_{across}^2 were estimated using empirical fMRI data. By estimating $\sigma_{\text{fMRI noise}}^2$, we can estimate $\sigma_{\text{(Stim,space)}}^2$ and $\sigma_{\text{(Stim,time)}}^2$ using Equations 4 and 5. To do this we need to estimate the characteristics of the fMRI noise. Unfortunately, common statistical models are not appropriate for describing fMRI noise, as the noise has been shown to be spectrally complex and variable from site to site within the brain

[Weisskoff et al., 1993; Biswal et al., 1996]. Consequently, in the next section, we use empirical estimates of fMRI noise to create simulated fMRI responses and estimate the delay variability caused by fMRI noise.

The simulated fMRI responses consisted of an ideal sinusoidal response of known amplitude added to empirically measured fMRI noise. In a simulation, fMRI responses were created using multiple samples of fMRI noise time series recorded during “fixation only” (control) scans and they were obtained only from voxels that, subsequently, would be activated by the visual stimulus. The sinusoid representing the ideal response had a constant delay (phase), and so, contributed nothing to the variance of the simulated response’s delay estimate. We assumed that the distribution of fMRI noise during stimulus presentation was the same as during the fixation-only condition and provide some supporting evidence below. Note

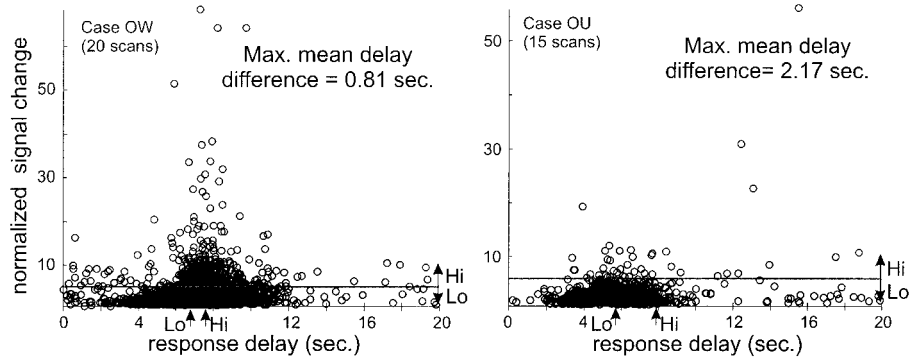


Figure 6.

Scatter plots of normalized fMRI signal change (S_n) vs. delay for the two most disparate subjects (positive responses only, stimulus cycle duration = 40 sec). The normalized signal change is expressed as a percentage of the baseline fMRI signal. For cases OW and OU, data were combined across 20 and 15 scan repetitions,

that we did not assume the distribution of fMRI noise to be Gaussian, white, or spatially independent.

The mathematical approach for creating the simulated fMRI responses was as follows. For voxel i , let $V_c(i)$ represent a sample of the noise time series. Let $V_a(i)$ represent the corresponding response during stimulus activation. To form a simulated response, $V_s(i)$, a sinusoid, $s(i)$ representing an ideal stimulus-induced response was added to the noise sample $V_c(i)$ such that:

$$V_s(i) = V_c(i) + s(i)$$

(6) The signal-to-noise ratio is defined as:

respectively. Horizontal lines show the threshold criterion that resulted in the largest difference in mean delay for high (Hi) vs. low (Lo) S_n responses. Markers on the abscissa indicate mean delays for each pool.

where: $s(i) = \alpha(i)\sin(2\pi f_c \cdot t + \phi)$
 f_c = stimulus cycle frequency (1/28, 1/40, 1/64 Hz)
 ϕ = true, constant response phase (delay)
 $\alpha(i)$ = the amplitude of $s(i)$, such that the signal-to-noise ratio (SNR) of $V_s(i)$ is equal to that of $V_a(i)$.

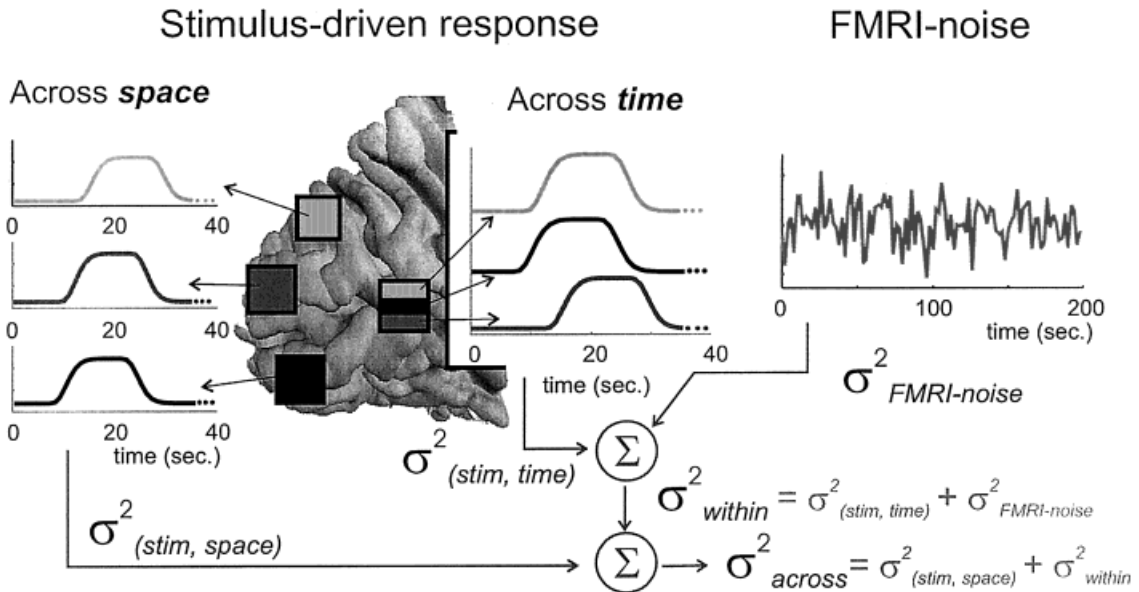


Figure 7.

Schematic of the contribution of fMRI noise ($\sigma_{FMRI\ noise}^2$) and stimulus-driven response variability to the empirical estimates of delay variance across voxels, σ_{across}^2 , and within voxels, σ_{within}^2 . The

stimulus-driven variability is broken down into variability across repeated measures at the same voxel location $\sigma_{(stim,time)}^2$ and variability across voxels $\sigma_{(stim,space)}^2$.

$$SNR = \frac{P(f_c)}{\sum_j P(f_j) - P(f_c)} \quad (7)$$

where: $P(f_j)$ = spectral power at frequency f_j .

The numerator represents the power in the signal at stimulus cycling frequency (f_c). The denominator represents the total power in the signal at all frequencies other than f_c .

In each simulation, $\sigma_{fMRI\ noise}^2$ was calculated from the delay estimates of the simulated fMRI responses. The number of simulated responses was equal to the number of voxels activated in the corresponding active scan (371 on average). The methods used to estimate the delays were exactly the same as those used in Part I to analyze the empirical data. Simulations were performed using a total of 10 control scans from three subjects.

PART II: SIMULATION RESULTS

Response delay variability resulting from fMRI noise

Figure 8 shows the distribution of response delays obtained from a set of simulated fMRI time series (light gray) and from empirical fMRI time series (dark gray) pooled across six scan repetitions. Across all

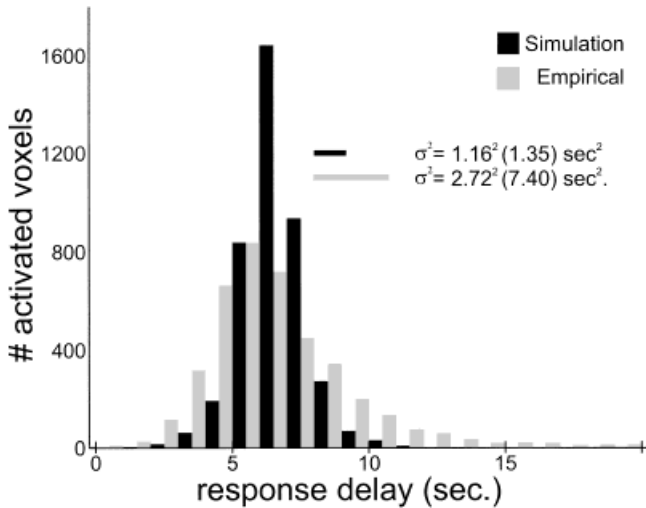


Figure 8.

Response-delay distributions obtained from empirical fMRI data (gray) and simulated data based on fMRI noise (black). The data were pooled from one subject, across six scan repetitions with stimulus cycle duration of 40 sec. The black and gray horizontal bars are graphical representations of the delay standard deviation for simulated and empirical data, respectively.

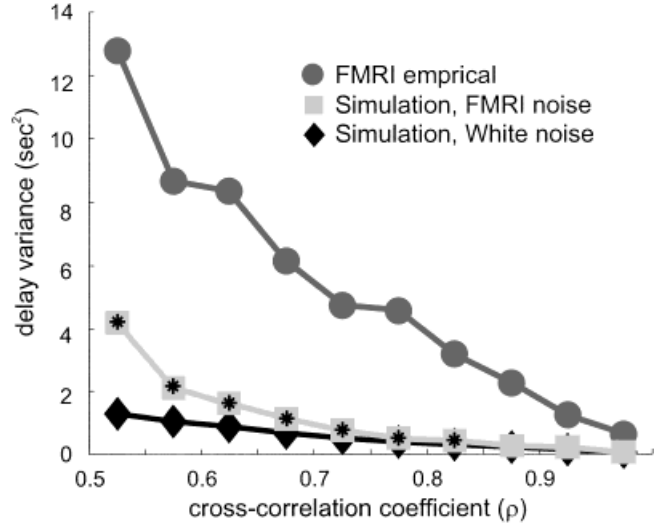


Figure 9.

Variance of the response delay as a function of cross-correlation coefficient (a measure of signal-to-noise ratio) for fMRI data (dark gray, circles), simulated data using fMRI noise (light gray, squares), and simulated data based on white noise (black, diamonds). The stars indicate significant differences in variance between white noise and fMRI noise (F-ratio test, $P < 0.01$). The data were pooled across three subjects.

subjects, the response delay variance for the simulated data was 1.45 sec^2 ($\sigma = 1.20 \text{ sec}$; range: 0.96–2.0) whereas the variance for the empirical data was 4.36 sec^2 ($\sigma = 2.09 \text{ sec}$; range: 1.26–2.88). Thus, 33% of delay variance (57% of standard deviation) was accounted for by the presence of fMRI noise. Using white noise in lieu of empirically measured fMRI noise significantly reduced the delay variance (variance ratio F test, $P < 0.001$). On average, the variance was reduced from 1.45 to 0.77 sec^2 , thereby underestimating the component of variance due to noise by nearly a factor of two.

Figure 9 shows how the delay variance changes as a function of the cross-correlation coefficient, ρ , used to identify statistically valid responses. Data are shown for the empirical fMRI data versus the simulated fMRI data based on sampled noise. For comparison, simulated data based on white noise are also shown. Using a variance ratio F test, we found that the variance was significantly larger for the empirical fMRI time series than for either of the two simulated time series ($P < 0.01$). At very high values of ρ (as signal-to-noise became large), the variance for all three data sets tended toward zero. At lower values of ρ (0.5–0.7), the delay variance was highest for the empirical data but was also significantly elevated for the simulated data based on fMRI noise. Note that for $\rho < 0.85$, the

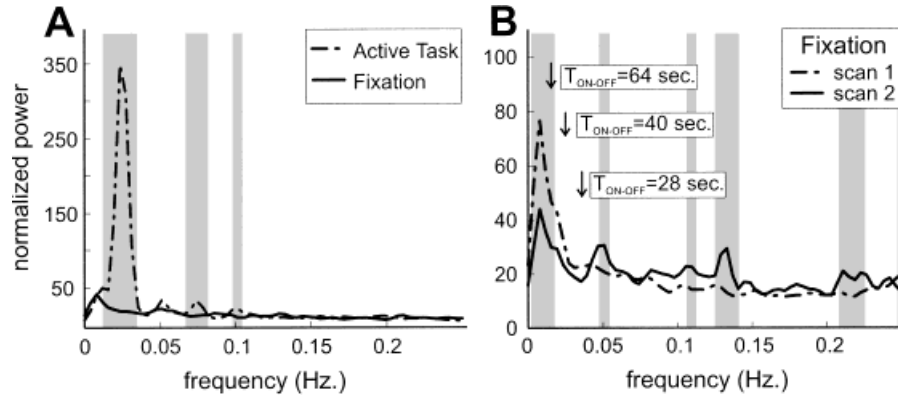


Figure 10.

(A): Average spectral power during active stimulus/task with 40-sec cycle (dashed) and during fixation only control (solid). (B): Example of average spectral power for two control (noise) scans obtained at different times in same experiment. Data from control scans such as these was used to estimate the spectral power of fMRI noise. Gray shading highlights bandwidths with significant

spectral power differences ($P < 0.001$) between the active task and fixation in (A) and between the two fixation scans in (B). Vertical arrows in (B) indicate noise power at same frequencies used for visual stimulus presentation. Note marked increase in noise power as stimulus frequency decreases. Also note different ordinate scales in (A) and (B).

variance resulting from fMRI noise was significantly larger (variance ratio F test, $P < 0.01$) than for white noise. At ρ between 0.5 and 0.55, the variance resulting from fMRI noise was 3.4 times larger than that from white noise. (ρ values of approximately 0.5 are typical criteria for acceptance of valid responses.)

The simulation was also carried out for stimuli having cycles ($T_{\text{ON-OFF}}$) of 28 and 64 seconds. The resulting delay variances differed significantly (variance ratio F test, $P < 0.01$) from the variances at $T_{\text{ON-OFF}}$ of 40 sec and were on average 0.54 sec^2 ($\sigma = 0.73 \text{ sec}$) and 4.25 sec^2 ($\sigma = 2.06 \text{ sec}$), respectively. Thus, delay variance induced by fMRI noise was proportional to $(T_{\text{ON-OFF}})^{2.5}$.

Stationarity of fMRI noise

The estimated contribution of fMRI noise to the delay variance is valid as long as the spectral content of the noise is stationary. In other words, the spectral content of noise in the control state must not change in the presence of cortical activation. Figure 10A illustrates the differences in average spectral power between active voxels (dashed) and the same voxels during the fixation only control condition (solid). The shaded segments highlight bandwidths at which the difference in spectral power was statistically significant ($P < 0.001$) [Kay, 1988]. Note that the largest differences in spectral power were at the stimulus cycle frequency ($1/40 = 0.025 \text{ Hz}$) and its harmonics (0.05, 0.075, and 0.1). (A separate simulation showed that differences in spectral power adjacent to the stim-

ulus frequency were spectral leakage artifacts inherent in the power spectrum estimation.) Similar results were obtained using different stimulation frequencies (1/64 and 1/28 Hz).

Note that during activation there is virtually no significant change in power other than at the stimulus fundamental frequency and its harmonics. Thus, activation does not appear to affect the fMRI signal in any nonspecific way, thereby lending some credence to the assumption of noise stationarity during activation. However, this does not necessarily preclude a selective mechanism that alters the noise only within the frequency bands occupied by the stimulus.

A second concern with respect to stationarity is whether the statistics of the noise are constant across repeated samples. Since respiration and aliased heart rate contribute significantly to the noise, there is reason to expect that the noise may change across samples. Figure 10B illustrates that successive noise samples can vary significantly. For example, at a stimulus period of 64 sec, the noise differed by 50% from one sample to the next. Because such spectral changes will alter the delay variability, the effects of fMRI noise should be assessed across multiple control scans.

Note that for different stimulus cycle durations, the noise power can vary significantly. In Figure 10B, arrows mark the noise components that would contribute to the variance of the stimulus-evoked responses for cycle durations of 64, 40, and 28 sec, respectively. Note the significant increase in noise power with increasing cycle duration.

Contributions of stimulus-driven responses

The components of delay variance are summarized in Table IB for the three different stimulus cycle durations. For stimuli with a 40-sec cycle, the measured within-voxel variance, σ_{within}^2 , and estimated noise variance, $\sigma_{\text{fMRI noise}}^2$, were used with Equation 4 to calculate the contribution due to changes in the stimulus driven response across time, $\sigma_{(\text{stim,time})}^2$. This contribution was not significantly different from zero because σ_{within}^2 and $\sigma_{\text{fMRI noise}}^2$ were found to be nearly identical (1.44 vs. 1.45 sec²). (Note that the estimates for $\sigma_{\text{fMRI noise}}^2$ and σ_{within}^2 were obtained from separate data sets.) Given the measurement error in the estimates of σ_{within}^2 and $\sigma_{\text{fMRI noise}}^2$, the value of $\sigma_{(\text{stim,time})}^2$ could have been as high as 0.64 sec² without being statistically different from zero.

Finally, using Equation 5 with $\sigma_{(\text{stim,time})}^2$ equal to 0, $\sigma_{(\text{stim,space})}^2$, was found to be 1.99, 2.91, and 19.21 sec² for stimulus cycles of 28, 40, and 64 sec, respectively.

DISCUSSION

In this study, we implemented an efficient algorithm for estimating fMRI response delays using the Hilbert transform. We then used this algorithm to describe the statistical distribution of delays for fMRI responses evoked in visual cortex by a cyclic pattern of visual stimulation. The mean delay for the activating responses was nearly 8.5 sec and varied little with the duration of the stimulus cycle period. In all 87 data sets analyzed, both positive and negative responses were observed.

Variability in empirical estimates of response delays

The estimated variance in response delay across a population of voxels, σ_{across}^2 , was 4.36 sec². This was three times larger than the variance within voxels, σ_{within}^2 . These results indicate that variability in the response delay throughout the brain is in large part because of fixed anatomical and/or physiological factors. Consequently, one might have expected the pattern of delays across the cortex to reflect known patterns of neural connectivity or synaptic delay. However, this did not appear to be the case.

One puzzling feature of the response delays was that the variance, σ_{across}^2 , increased as the stimulus cycle lengthened, even though the mean delay remained unchanged (Table IA). This appears to be at least partly the result of the unique characteristics of fMRI noise. The power spectrum of fMRI noise is not

uniform like white noise. Rather, the power of fMRI noise increases at lower temporal frequencies, especially over the range of stimulus frequencies (or cycle durations) used in this study, and in many published studies. The effect of noise added to the fMRI response is to introduce variance in the phase spectrum, that is, to add to the delay variability. For a sinusoidal signal, delay (δ) and phase (ϕ) at a frequency F are related by $\delta = \phi/(2\pi F)$. Consequently, we expected that the delay variance would be related to noise as a function of $1/F^\beta$. For white noise, $\beta = 2$ as phase variability is constant at all frequencies. However, given the increase in fMRI noise power with decreasing frequencies, we expected β to be larger than 2. Indeed, from our simulation data, the average empirical estimate of β was 2.5. This dependence of the delay variance on stimulus cycle was to be expected given the properties of fMRI noise. Moreover, it suggests that more accurate delay estimates can be obtained by presenting stimuli and tasks in a block design with the shortest viable cycle duration.

Variability of stimulus-induced response delays

After accounting for the contribution of fMRI noise, we found that, on average, the stimulus-induced delay variance over time, $\sigma_{(\text{stim,time})}^2$, was not measurably different from zero. In other words, once the contribution of fMRI noise was factored out, the fMRI response delay was found to be constant across repeated stimulus presentations. Nevertheless, there must have been some variability in the underlying neural events. Given the range of variability in our estimates of σ_{within}^2 and $\sigma_{\text{fMRI noise}}^2$, this component could not have been larger than 0.64 sec². Indeed, available evidence suggests that $\sigma_{(\text{stim,time})}^2$, estimated from average fMRI responses, is on the order of 0.07 sec² and as low as 0.005 sec² [Menon et al., 1998; Saad et al., 1999a, 1999b].

Although the trend toward increasing delay variance observed in our empirical measurements of σ_{across}^2 was partly accounted for by the fMRI noise, there remained an additional component, $\sigma_{(\text{stim,space})}^2$, that also increased with cycle duration (Table IB). This remaining component was caused by the presence of voxels activated at longer, but not shorter, stimulus cycle durations. Such voxels typically had longer delays and lower signal-to-noise ratios than voxels activated by all cycle durations. Consequently, the addition of these extra voxels to the distribution resulted in the increased variance. Thus, the spatial variance appeared to be somewhat higher for longer stimulus cycle durations.

Stationarity assumptions

The algorithm we used to estimate response delays assumes that the fMRI response to a stimulus is invariant both in time and space, except for a fixed time delay between stimulus and response. Theoretically, portions of the fMRI response such as the onset should suffice for estimating the true response delay at a certain voxel. In practice, the entire fMRI response time series is used to reduce the variability introduced by noise of the estimated response delays [Saad et al., 1999b]. However, use of the entire fMRI response could result in increased delay variability if the temporal and spatial stationarity condition is violated. The source of such variability could be neuronal, cognitive, or hemodynamic in origin. For example, fluctuations in the subject's attention during the ON period of a stimulus would introduce nonstationarity in the response. In a recent publication, Menon and colleagues [1998] remarked that only the onset of the fMRI response to a stimulus is stationary across space and time and that the remainder of the time series is more variable. However, in a separate analysis [Saad et al., 1999b] we found that the use of the entire fMRI response resulted in significantly lower variance in estimated delay than the use of the rising phase as suggested Menon and colleagues [1998].

Response delays for vessels vs. parenchyma

We have shown that most of the variability in response delays occurs across spatial locations. In the literature [Lai et al., 1993; Lee et al., 1995], such spatial variability is attributed to large veins that drain activated areas. Lee and colleagues [1995] found that draining vessels can produce fMRI responses with delays between 8 and 14 sec. This is in contrast to the 4–8-sec delay they observed for parenchymal tissue. In part, our results and those by Kruggel and von Cramon [1999b] were consistent with these observations. Responses in blood vessels identified by 2D-TOF imaging or by large signal change were delayed with respect to responses in parenchyma. However, in our data, the delay difference was on the order of 1–2 sec and not longer. This is in excellent agreement with the result reported by Kruggel and von Cramon [1999b] who examined response delays differences between voxels in the vicinity of the great cerebral vein and nine other cortical ROIs during a language processing task. Across all ROIs, they found delay differences ranging between 0.45 and 3.27 sec with a mean of 1.6 sec. Overall, we found a large overlap of delays for the parenchyma and blood vessels. Our data do

not support the contention that all voxels with large delays are mapped to large draining veins. Hence, it may not be valid to assume that all voxels with long delays are artifactual. The only caveat to this conclusion is that our methods for classifying voxels as blood vessels or parenchyma may not be perfect. Consequently, we cannot entirely reject the possibility that a portion of the overlap in delay is the result of misclassification. However, it is important to note that we did not bias our analysis by manually selecting a population of blood vessels and measuring their response delays. Rather we obtained an unbiased separation of the two pools by using a continuum of thresholds and seeking maximal delay differences between the two pools.

Because our data suggests that the spatial variability in response delay was only partly the result of venous drainage, it follows that the parenchyma must contribute significantly to this variance. This conclusion is bolstered by results from Moskalenko and colleagues [1996a] who used the hydrogen clearance method to study delays in rat whisker barrel cortex. This method is selectively sensitive to local parenchymal blood flow [Moskalenko et al., 1996b] and yielded a range of approximately 6 sec in response delays. Moreover, Moskalenko obtained a delay variance of 2.56 sec^2 ($\sigma = 1.6 \text{ sec}$), which is in close agreement with our own measurements.

Mechanisms resulting in negative fMRI responses

The physiological origins of negative fMRI responses are poorly understood. Examination of these signals relative to a prestimulus baseline showed that they were truly suppressive, that is, the signal fell below baseline during stimulus presentation and then returned to baseline during the control period. Thus, negative responses were not the result of activating responses that were delayed by half the stimulus cycle. It was also clear that both activating and suppressive signals occurred within cortex associated with a single modality (vision). Haxby had suggested that they might primarily occur as an interaction between sensory modalities [Haxby et al., 1994].

Several mechanisms might contribute to the occurrence of negative responses. These include frequency shift artifacts, local fixed differences in physiological properties, venous drainage delays, attentional modulation, neuronal deactivation or inhibition, and blood flow redistribution. Our data allow us to reject the first four alternatives as the primary basis for negative responses. Frequency shift artifacts cause negative fMRI responses only in voxels that are immediately

adjacent to voxels with strong activating responses [Jesmanowicz et al., 1993]. Our delay maps clearly show negative responses in large homogenous patches containing many voxels that were not adjacent to positive voxels. Many voxels within the visual cortex were suppressed by one stimulus but activated by another. Consequently, these negative responses are not associated with peculiar, fixed physiological differences at certain brain sites [Shulman et al., 1997], nor are they primarily associated with delayed “downstream” signals from draining veins. One could imagine that attentional activation [Kastner et al., 1998; Tootell et al., 1998; Brefczynski and DeYoe, 1999; Somers et al., 1999] directed to the fixation point during the stimulus OFF periods might have created a signal that was apparently phase shifted by half the stimulus cycle or that was suppressive at nonattended sites. However, voxels with negative responses were found even when subjects were required to constantly attend to the fixation point throughout the sequential ON-OFF presentation of the checkered annulus. Given these considerations, two alternatives remain: either the negative responses reflect true neural events within and across sensory modalities or they reflect blood flow redistribution whereby increased blood flow in areas of intense activation causes reduced flow in neighboring areas [Seitz et al., 1992; Cox et al., 1993; Haxby et al., 1994; Lee et al., 1995; Moskalkenko et al., 1996a; Woolsey et al., 1996; Shulman et al., 1997]. The available data do not allow us to reject either alternative.

ACKNOWLEDGMENTS

The authors thank Drs. B. Anderson, M. Beauchamp, B. Biswal, and S. Glickman, J. Kummer, and J. Wieser for valuable advice and technical assistance. This work was supported by NIH grant EY10244 and MH51358 to E.A. DeYoe, a predoctoral fellowship to Ziad Saad from a Whitaker Foundation Special Opportunity Award, and by an Anthony J. and Rose Eanelli Bagozzi Medical Research Fellowship to K. M. Ropella. Support was also provided by NIH grant GCRC1234 to the general clinical research center at the Medical College of Wisconsin.

REFERENCES

- Backfrieder W, Baumgartner R, Samal M, Moser E, Bergmann H (1996): Quantification of intensity variations in functional MR images using rotated principal components. *Phys Med Biol* 41: 1425–1438.
- Bandettini PA, Jesmanowicz A, Wong EC, Hyde JS (1993): Processing strategies for functional MRI of the human brain. *Magn Reson Med* 30:161–173.
- Bendat JS, Piersol AG (1986): *Random data: analysis and measurement procedures*. New York: Wiley.
- Bendat JS, Piersol AG (1993): *Engineering applications of correlation and spectral analysis*. New York: Wiley.
- Biswal B, DeYoe EA, Hyde JS (1996): Reduction of physiological fluctuations in fMRI using digital filters. *Magn Reson Med* 35:107–113.
- Biswal B, Zerrin YF, Haughton VM, Hyde JS (1995): Functional connectivity in the motor cortex of resting human brain using echo-planar MRI. *Magn Reson Med* 34:537–541.
- Brefczynski JA, DeYoe EA (1999): A physical correlate of the ‘spotlight’ of visual attention. *Nat Neurosci* 2:370–374.
- Buchner H, Weyen U, Frackowiak R, Romaya J, Zeki S (1994): The timing of visual evoked potential activity in human area V4. *Proc R Soc Lond B Biol Sci* 257:99–104.
- Bullier J, Hupe J, James A, Girard P (1996): Functional interactions between areas V1 and V2 in the monkey. *J Physiol* 90:217–220.
- Cox RW, Hyde JS (1997): Software tools for analysis and visualization of fMRI data. *NMR Biomed* 10:171–178.
- Cox SB, Woolsey TA, Rovainen CM (1993): Localized dynamic changes in cortical blood flow with whisker stimulation corresponds to matched vascular and neuronal architecture of rat barrels. *J Cereb Blood Flow Metab* 13:899–913.
- DeYoe EA, Bandettini P, Neitz J, Miller D, Winans P (1994): Functional magnetic resonance imaging (fMRI) of the human brain. *J Neurosci Meth* 54:171–187.
- DeYoe EA, Carman G, Bandettini P, Glickman S, Wieser J, Cox R, Miller D, Neitz J (1996): Mapping striate and extrastriate visual areas in human cerebral cortex. *Proc Natl Acad Sci U S A* 93:2382–2386.
- Engel S, Glover G, Wandell B (1997): Retinotopic organization in human visual cortex and the spatial precision of functional MRI. *Cereb Cortex* 7:181–192.
- Engel SA, Rumelhart DE, Wandell BA, Lee AT, Glover GH, Chichilnisky E, Shadlen MN (1994): fMRI of human visual cortex. *Nature* 369:525.
- Engel SA, Wandell BA, Rumelhart DE, Lee AT, Shadlen MN, Chichilnisky EJ, Glover GH, Newsome WT (1993): Functional MRI measurements of human striate cortex topography. *Soc Neurosci Abs* 19:335.
- Forman S, Cohen J, Fitzgerald M, Eddy W, Mintun M, Noll D (1995): Improved assessment of significant activation in functional magnetic resonance imaging (fMRI): use of a cluster-size threshold. *Magn Reson Med* 33:636–647.
- Friston KJ, Frith CD, Liddle PF, Dolan RJ, Lammertsma AA, Frackowiak RS (1990): The relationship between global and local changes in PET scans. *J Cereb Blood Flow Metab* 10:458–466.
- GE Medical Systems (1990): *Vascular magnetic resonance imaging*. In: Turski P, editor. *SIGNA applications guide*. Milwaukee, WI: Author, p 48.
- Haxby JV, Horwitz B, Ungerleider LG, Maisog JM, Pietrini P, Grady CL (1994): The functional organization of human extrastriate cortex: a PET-rCBF study of selective attention to faces and locations. *J Neurosci* 14:6336–6353.
- Hogg RV, Ledolter J (1987): *Engineering statistics*. New York: Macmillan.
- Jesmanowicz A, Bandettini PA, Hyde JS (1993): Frequency shift artifacts in functional echo planar imaging. *Proc Soc Magn Reson Med*. New York, New York: Vol. 1, p 437.

- Johnson RA, Wichern DW (1992): Applied multivariate statistical analysis. Englewood Cliffs, NJ: Prentice-Hall.
- Kastner S, De Weerd P, Desimone R, Ungerleider L (1998): Mechanisms of directed attention in the human extrastriate cortex as revealed by functional MRI. *Science* 282:108–111.
- Kay SM (1988): Modern spectral estimation: theory and application. Englewood Cliffs, NJ: Prentice-Hall.
- Kruggel F, von Cramon DY (1999a): Modeling the hemodynamic response in single-trial functional MRI experiments. *Magn Reson Med* 42:787–797.
- Kruggel F, von Cramon DY (1999b): Temporal properties of the hemodynamic response in functional MRI. *Hum Brain Mapp* 8:259–271.
- Lai S, Hopkins AL, Haacke EM, Li D, Wasserman BA, Buckley P, Friedman L, Meltzer H, Hedera P, RF (1993): Identification of vascular structure as a major source of signal contrast in high resolution 2D and 3D functional activation imaging of the motor cortex at 1.5 T: preliminary results. *Magn Reson Med* 30:387–392.
- Lee AT, Glover GH, Meyer CH (1995): Discrimination of large venous vessels in time-course spiral blood-oxygen-level-dependent magnetic-resonance functional neuroimaging. *Magn Reson Med* 33:745–754.
- Menon RS, Luknowsky DC, Gati JS (1998): Mental chronometry using latency-resolved functional MRI. *Proc Natl Acad Sci* 95:10902–10907.
- Menon RS, Ogawa S, Tank DW, Ugurbil K (1993): Four Tesla gradient recalled echo characteristics of photic stimulation induced signal changes in the human primary visual cortex. *Magn Reson Med* 30:380–386.
- Mitra P, Ogawa S, Hu X, Ugurbil K (1997): The nature of spatiotemporal changes in cerebral hemodynamics as manifested in functional magnetic resonance imaging. *Magn Reson Med* 37:511–518.
- Moskalenko Y, Dowling J, Liu D, Rovainen C, Semernia V (1996a): LCBF changes in rat somatosensory cortex during whisker stimulation monitored by dynamic H₂ clearance. *Intl J Psychophysiol* 21:45–59.
- Moskalenko Y, Rovainen C, Woolsey T, Wei L, Lui D, Spence M, Semernia V, Weinstein G, Malysheva N (1996b): Comparison of measurements of local brain blood flow by hydrogen clearance with the inhalation of hydrogen and its electrochemical generation in brain tissue. *Neurosci Behav Physiol* 26:245–250.
- Nowak L, Bullier J (1997): The timing of information transfer in the visual system. *Cereb Cortex* 12:205–241.
- Ogawa S, Menon RS, Tank DW, Kim S-G, Merkle H, Ellerman JM, Ugurbil K (1993): Functional brain mapping by blood oxygenation level-dependent contrast magnetic resonance imaging. *Biophys J* 64:803–812.
- Rao SM, Binder JR, Biswal BB, Hammeke TA, O'Farrell AM, Bobholz JH (1995): Functional MRI demonstrates temporal patterns of brain activation during sequential finger movements. *J Intl Neuropsych Soc* 1:371.
- Saad Z, DeYoe E, Ropella K (1999a): Variance in fMRI activation delays: methodological or physiological? Fifth International Conference on Functional Mapping of the Human Brain. Dusseldorf, Germany. Vol. 1, p 89.
- Saad ZS (1996): Functional magnetic resonance imaging: activated time course detection and phase analysis [master's thesis]. Milwaukee, WI: Marquette University.
- Saad ZS, Carman GJ, DeYoe EA (1995): Temporal variation of fMRI signals. *Proc Soc Magn Reson Med*. Nice, France. Vol. 1, p 813.
- Saad ZS, DeYoe EA, Ropella KM (1997a): High resolution time delay estimation of fMRI signals using the hilbert transform. *Proc ISMRM, 5th Scientific Meeting and Exhibition*. Vancouver, Canada. Vol. 1, p 1673.
- Saad ZS, DeYoe EA, Ropella KM (1997b): Time delay estimates of fMRI signals: efficient algorithm and estimate variance. *Proc 19th Annual International Conference IEEE/EMBS*. Chicago, Illinois. Vol. 1, p 460–463.
- Saad ZS, Ropella KM, Carman GJ, DeYoe EA (1996): Temporal phase variation of fMRI signals in vasculature versus parenchyma. *Proc Soc Magn Reson Med*. New York, New York. Vol. 1, p 1834.
- Saad ZS, Ropella KM, DeYoe EA (1997c): Estimating temporal phase variance in fMRI time courses. *Proc ISMRM 5th Scientific Meeting and Exhibition*. Vancouver, Canada. Vol. 1, p 1674.
- Saad ZS, Ropella KM, DeYoe EA (1999b): On the estimation of neural latencies with fMRI. *Proc Soc Neurosci*. Miami, FL. 25: 1549.
- Schmolecky M, Wang Y, Hanes D, Thompson K, Leutgeb S, Schall J, Leventhal A (1998): Signal timing across the macaque visual system. *J Neurophysiol* 79:3272–3278.
- Seitz RJ, Roland E, Bohm C, Greitz T, Stone-Elander S (1990): Motor learning in man: a positron emission tomographic study. *Neuroreport* 1:57–60.
- Seitz RJ, Roland PE (1992): Vibratory stimulation increases and decreases the regional cerebral blood flow and oxidative metabolism: a positron emission tomography (PET) study. *Acta Neurol Scand* 86:60–67.
- Sereno MI, Dale AM, Reppas JB, Kwong KK, Belliveau JW, Brady TJ, Rosen BR, Tootell RBH (1995): Borders of multiple visual areas in humans revealed by functional MRI. *Science* 268:889–893.
- Shulman GL, Fiez JA, Corbetta M, Buckner RL, Miezin FM, Raichle ME, Petersen SE (1997): Common blood flow changes across visual tasks: II. Decreases in cerebral cortex. *J Cogn Neurosci* 9:648–663.
- Somers D, Dale A, Seiffert A, Tootell R (1999): Functional MRI reveals spatially specific attentional modulation in human primary visual cortex. *Proc Natl Acad Sci U S A* 96:1663–1668.
- Strother SC, Anderson JR, Schaper KA, Sidtis JJ, Liow JS, Woods RP, Rottenberg DA (1995): Principal component analysis and the scaled subprofile model compared to intersubject averaging and statistical parametric mapping: I. "Functional connectivity" of the human motor system studied with [15O]water PET. *J Cereb Blood Flow Metab* 15:738–753.
- Tootell R, Hadjikhani N, Hall E, Marrett S, Vanduffel W, Vaughan J, Dale A (1998): The retinotopy of visual spatial attention. *Neuron* 21:1409–1422.
- Weisskoff RM, Baker J, Belliveau J, Davis TL, Kwong KK, Cohen MS, Rosen BR (1993): Power spectrum analysis of functionally-weighted MR data: What's in the noise? *Proc Soc Magn Reson Med* 1:7.
- Wong EC, Bandettini PA, Hyde JS (1992): Echo-planar imaging of the human brain using a three axis local gradient coil. *Proc Soc Magn Reson Med* 1:105.
- Woolsey T, Rovainen C, Cox S, Henegar M, Liang G, Liu D, Moskalenko Y, Sui J, Wei L (1996): Neuronal units linked to microvascular modules in cerebral cortex: response elements for imaging the brain. *Cereb Cortex* 6:647–660.

APPENDIX: ESTIMATION OF RESPONSE DELAYS USING THE HILBERT TRANSFORM

The Hilbert Transform $H[s(t)]$ of a real valued function $s(t)$ is the convolution of $s(t)$ with $1/\pi t$. The transform leaves the amplitude spectrum of $s(t)$ un-

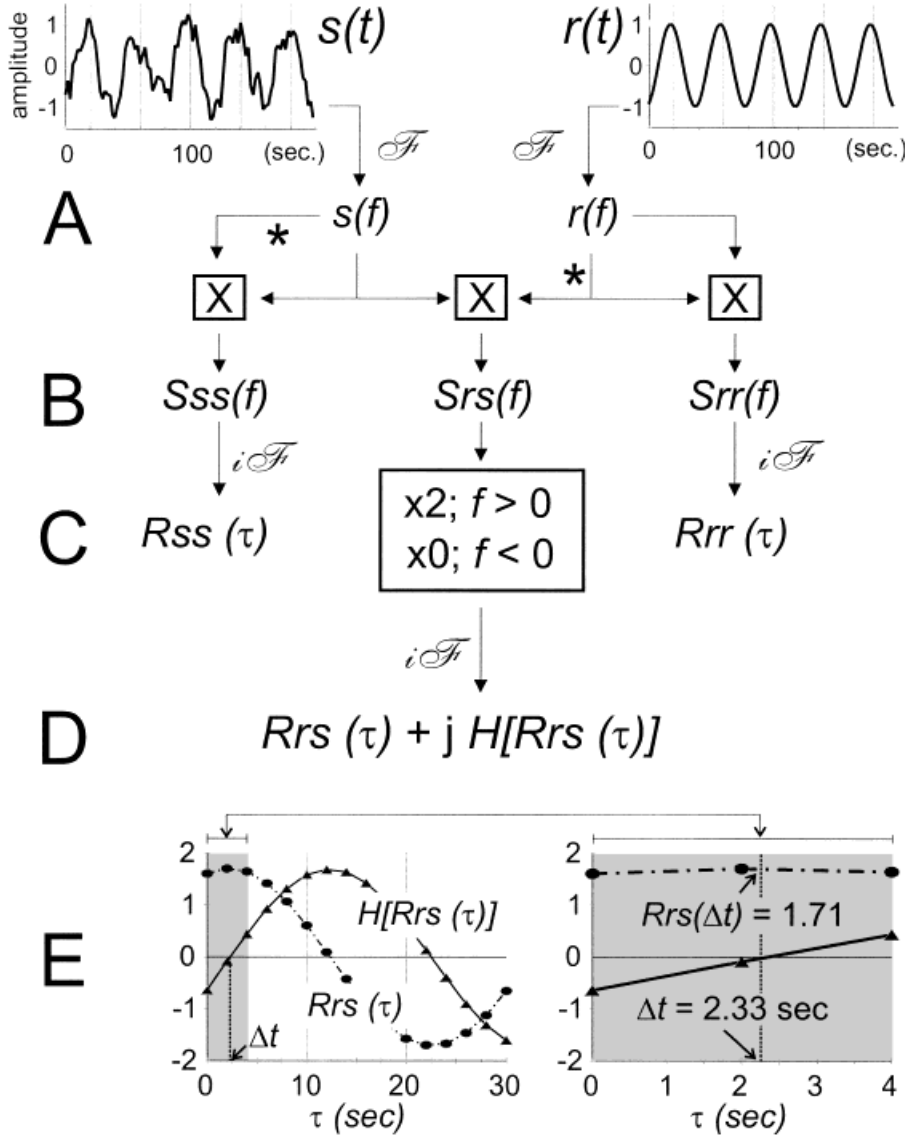


Figure 11.

Outline of computations used to estimate response delay (Δt) and cross-correlation coefficient $\rho_{rs}(\Delta t)$ between the fMRI signal $s(t)$ and the reference signal $r(t)$ (see appendix for details). The graph on the bottom left shows the cross-correlation function $R_{rs}(\tau)$ and its Hilbert transform $H[R_{rs}(\tau)]$. The graph portion for τ between 0 and 4 sec is enlarged on the right. \mathcal{F} = Fast Fourier Transform; $i\mathcal{F}$ = inverse \mathcal{F} ; * = complex conjugate; $R_{..}(\tau)$ = correlation function; $S_{..}(f)$ = power spectrum.

changed but changes the positive frequency phase spectrum by $\pi/2$ and the negative frequency phase spectrum by $-\pi/2$ [Bendat et al., 1993]. The cross-correlation function $R_{rs}(\tau)$, describes the correlation between $r(t)$ and $s(t + \tau)$ for a range of a time delay (τ) between the two signals. It can be shown that when τ is equal to the response delay Δt , the cross-correlation function $R_{rs}(\tau)$ is maximal and $H[R_{rs}(\tau)]$ is equal to zero. The same is true for the cross-correlation coefficient function $\rho(\tau)$, which is a normalized form of $R_{rs}(\tau)$. Finding the point of zero crossing of $H[\rho(\tau)]$ is computationally easier than finding the maximum of $\rho(\tau)$. The computation of $\rho(\tau)$ and $H[\rho(\tau)]$ in the time domain are computationally expensive since they involve convolutions. However, by making use of the properties of analytic signals (the analytic signal $Z_s(t)$

of $s(t)$ is given by: $Z_s(t) = s(t) + jH[s(t)]$) and their corresponding cross-power spectra, we can compute $\rho(\tau)$ and $H[\rho(\tau)]$ via Fast Fourier Transform operations as outlined in Figure 11 and below.

- A. Compute the Fast Fourier Transform $s(f)$ and $r(f)$ of the fMRI response $s(t)$ and the reference signal $r(t)$, respectively.
- B. Use $s(f)$ and $r(f)$ to compute the cross-power spectrum $S_{rs}(f)$ of $s(t)$ and $r(t)$ and their autospectra $S_{rr}(f)$ and $S_{ss}(f)$.
- C. Compute the inverse Fast Fourier Transform of $S_{rr}(f)$ and $S_{ss}(f)$ to obtain the autocorrelation functions $R_{rr}(t)$ and $R_{ss}(t)$ of $s(t)$ and $r(t)$, respectively.
- D. Multiply $S_{rs}(f)$ by 2 for positive frequencies and

0 for negative frequencies. The inverse Fast Fourier Transform of the modified $S_{rs}(f)$ is a complex series having the cross-correlation function $R_{rs}(\tau)$ and its Hilbert Transform $H[R_{rs}(\tau)]$ as its real and imaginary parts, respectively.

- E. Interpolate using $H[R_{rs}(\tau)]$ around the first 0 crossing to estimate the response delay Δt such that $H[R_{rs}(\Delta t)] = 0$. Interpolate using $R_{rs}(\tau)$ around Δt to estimate $R_{rs}(\Delta t)$.
- F. Estimate the cross-correlation coefficient $\rho(\Delta t)$

using Equation 3 in the text and Δt obtained in E.

The cross-correlation coefficient, which is used to determine if a voxel is activated, is maximal at the time delay between the reference and fMRI time series. The algorithm was implemented as a plug-in for MCW-AFNI software package [Cox et al., 1997] and is freely available by request from the authors.